Title

Atomistic modeling of La 3+ doping segregation effect on nanocrystalline yttria-stabilized zirconia

Journal

Physical Chemistry Chemical Physics, 20(19)

ISSN

0956-5000

Authors

Zhang, Shenli
Sha, Haoyan
Castro, Ricardo HR
et al.

Publication Date

2018-05-16

DOI

10.1039/c8cp02010h

Peer reviewed

Atomistic modeling of La^{3+} doping segregation effect on nanocrystalline yttria-stabilized zirconia

Shenli Zhang[1], Haoyan Sha[2], Ricardo H. R. Castro[1] and Roland Faller[2*]

[1] Department of Materials Science and Engineering, University of California, Davis, Davis, CA 95616, USA

[2] Department of Chemical Engineering, University of California, Davis, Davis, CA 95616, USA

ABSTRACT

The effect of La^{3+} doping on the structure and ionic conductivity change in nanocrystalline yttria-stabilized zirconia (YSZ) was studied using a combination of Monte Carlo and molecular dynamics simulations. The simulation revealed the segregation of La^{3+} at eight tilt grain boundary (GB) structures and predicted an average grain boundary (GB) energy decrease of 0.25 J/m^2, which is close to experimental values reported in the literature. Cation stabilization was found to be the main reason for the GB energy decrease, and energy fluctuations near the grain boundary are smoothed out with La^{3+} segregation. Both dynamic and energetic analysis on Σ13 (510)/[001] GB structure revealed La^{3+} doping hinders O^{2-} diffusion in the GB region, where the diffusion coefficient monotonically decreases with increasing La^{3+} doping concentration. The effect was attributed to the increase in the site-dependent migration barriers for O^{2-} hopping caused by segregated La^{3+}, which also leads to anisotropic diffusion at the GB.

Keywords

Atomistic simulation; Grain boundaries; Grain boundary segregation; Ionic diffusion

1. Introduction

YSZ is widely used as electrolyte material for solid oxide fuel cells (SOFC) due to its relatively high ionic conductivity. There has been significant interest from the community on the

*Corresponding author. Tel: +1 530 752-5839.
E-mails: rfaller@ucdavis.edu (R. Faller), shlzhang@ucdavis.edu (S. Zhang), hsha@ucdavis.edu (H. Sha), rhrcastro@ucdavis.edu (R. Castro)

manufacturing of nanocrystalline YSZ for SOFC applications owing to the expected higher ion exchange rates when directly applying the setup to the electrode at the fuel cell [1, 2]. Such effect shall overcome the detrimental impacts of the extensive grain boundary volume in terms of the reduction of ionic conductivity. One fundamental challenge on the manufacturing of nanocrystalline YSZ is its inherent instability due to the excess energies emerging from the extensive grain boundary network. Targeting a decrease in the excess energy by exploiting dopant segregation at the grain boundary (GB) has been proposed as a potential solution for this problem [3-5]. Its effectiveness has been investigated in a few experimental studies [6, 7] showing that by doping YSZ with an additional trivalent cation can decrease the GB energy and suppress grain coarsening during manufacturing of the material.

However, it is still unclear how a trivalent dopant in addition to Y^{3+}, such as La^{3+}, affects the local atomic structure at the grain boundary that leads to the reduced excess energy. Atomistic simulation is an effective tool to address these questions. Simulation techniques such as Monte Carlo (MC) [8, 9] and hybrid molecular dynamics-Monte Carlo MD-MC [10] have been applied to understand Y^{3+} behavior at ZrO_2 GB. The distribution of Y^{3+} was determined, and its segregation mechanism at the GB was proposed, where stabilization of cations [9] and a high concentration of oxygen vacancies at GB [8, 10] have been found as main factors. The role of grain boundaries with Y^{3+} segregation on the ionic conductivity of YSZ has also been widely studied using atomistic simulation [11-17]. Fisher et al. [11] reported a decrease in the ionic conductivity of YSZ due to yttrium segregation at the GBs, and Krishnamurthy et al. [14] found correlation effects for oxygen diffusion with increasing yttrium concentration. González-Romero [12, 13] observed segregation affects bulk diffusion of oxygen, but not GB diffusion. In the general, the discussion of Dilpuneet et al. [15] on

dopant effects to ionic conductivity points out the choice of dopants for better conductivity requires a balance between segregation, binding and migration energies. Studies on second dopants have also been conducted. For example, Xie et al. [18] found by introducing Gd_2O_3 into YSZ, the total conductivity could be improved at low temperatures.

In this paper, we further extend the study to a La_2O_3-doped YSZ using atomistic simulations to understand the La^{3+} stabilization effect on GB and its influence on ionic conductivity. The first part of the paper focuses on the dopant distribution and grain boundary energy change with La^{3+} doping. MC simulation was used to equilibrate various GB configurations with different tilt angles and tilt axes. The second part uses molecular dynamics (MD) simulation to characterize ionic conductivity at the specific Σ13 (510)/[001] GB. Diffusion coefficients at different temperature and La^{3+}/Y^{3+} doping ratios were obtained. Nudged elastic band (NEB) calculations were performed to characterize the anionic hopping energy barrier across La^{3+} and Y^{3+} dopants, and their formation energy with oxygen vacancy were also compared. The understanding of this La_2O_3-doped YSZ system will help to obtain better properties of nanocrystalline YSZ with dopant modulation.

2. Methods

2.1. Force field parameters

The interaction between cations and anions was treated as fully ionic, modeled by a short-range Born-Mayer-Buckingham (BMB) potential and the long-range Coulomb potential (eq.1)

$$E = Ae^{-r/\rho} - \frac{C}{r^6} + \frac{1}{4\pi\varepsilon_0}\frac{q_1 q_2}{r} \quad \text{eq.1}$$

Here A, ρ and C are empirical parameters shown in Table 1 [19], r is the distance between two ions, and q_i the charge of ion i. The cutoff distance for short range interaction was 10 Å. This potential

is chosen based on the ionic bonding nature in our materials. The short-range interaction captures the repulsive energy from the overlapping of electron orbitals ($Ae^{-r/\rho}$), and attractive energy from dispersion interaction ($-\frac{C}{r^6}$). Coulombic force among the ions is included in the long-range interaction. Therefore, this model describes all essential interaction types in the material. The potential parameters used here have been proven to reasonably reproduce the cubic structure of YSZ, as well as those of other M_2O_3 compounds [19].

Table 1 Buckingham potential parameters[19]

Species Pair	**A(eV)**	**ρ (Å)**	**C (eV Å^6)**
O^{2-} -O^{2-}	9547.96	0.2192	32
Zr^{4+} -O^{2-}	1502.11	0.3477	5.1
Y^{3+} -O^{2-}	1766.40	0.33849	19.43
La^{3+} -O^{2-}	2088.79	0.3460	23.25

2.2. GB model construction

In this study, GB models are confined to the symmetric tilt type. Two tilt directions ([001] and [110]) were considered, each sampled with different tilt angles. The detailed GB parameters including tilt direction, tilt angle, unit cell size and number of atoms are provided in Supporting Table S1. GB structures are formed by rotating two grains about the tilt direction (set as the z axis) by half of their tilt angle. x and z axes form the GB plane (hkl), and the y axis is perpendicular to the GB plane. Overlapping atoms (with distances <0.3 Å) due to rotation have been deleted.

The initial crystal phase is cubic ZrO_2 with a lattice constant $a = 5.07$ Å, YSZ and La^{3+} doping in YSZ is realized by random substitution of Zr^{4+} (below). Periodic boundary conditions are applied in all three directions, and the length of the simulation box is set that it ensures integer multiples of $a\sqrt{{h_i}^2 + {k_i}^2 + {l_i}^2}$ in the corresponding i axis ([h_i, k_i, l_i] denote the axes direction in the basis of the lattice vectors). Due to the boundary conditions, there are two grain boundaries in the

system. Following previous literature [9, 20-22], for ions that are of the same charge type and very close to each other at the GB, further modification is performed to avoid strong repulsion, i.e., deleting one of the ions and then center the remaining ion at the GB plane. Charge neutrality is maintained. Structure relaxation is then performed using steepest descent in LAMMPS [23].

The two GB regions are not fully identical in various characterizations (e.g., Fig.1 and Fig.3), possibly because the numerical precision of the simulation box length was set to 10^{-4}, which leads to some error comparing to theoretical integer multiples of $a\sqrt{{h_i}^2 + {k_i}^2 + {l_i}^2}$. Structure relaxation and MC equilibration further magnify the initial small difference and lead to asymmetrical results. Qualitative conclusions are not affected from the results.

2.3. Doping configuration

The molar concentration of doped oxides is defined as $\frac{M_2O_3}{M_2O_3+ZrO_2}$, where M stands for trivalent cations. The total concentration of M_2O_3 is fixed at 10 % to keep a constant oxygen vacancy concentration. In our nomenclature, 10YSZ means 10% Y_2O_3 doping and 8.5Y1.5La means 8.5% Y_2O_3 and 1.5% La_2O_3 doping. Three independent configurations were generated for each doping case by random substitution of Zr^{4+} and random deletion of O^{2-}.

The optimization and equilibration of the initial structures were performed using Monte Carlo (MC) in TOWHEE [24] under NVT (T = 300 K). Two MC moves were used, swap among cations with equal probability and translation of ions (O^{2-} have higher translation probability, because they diffuse much faster than cations). During each MC move, the energy of the new configuration is calculated and accepted with probability of min(1, $\exp(\frac{-\Delta E}{k_B T})$). ΔE is the energy difference before and after the move, k_B is Boltzmann's constant and T is temperature.

The equilibration time of our system is on the order of 10^8 steps. The acceptance rate of swap between Zr^{4+} and doping cations is around 10^{-4}, while that between trivalent cations can be around 10^{-2}. Data generated during the production stage of another 10^8 steps is used for analysis. Bulk structures of each doping case are also generated in the same way for GB energy calculation.

2.4. Molecular dynamics and Nudged elastic band calculation

Mean square displacements (MSD) of O^{2-} ions were calculated using molecular dynamics simulation in LAMMPS [23], defined as

$$MSD = \frac{1}{N}\sum_1^N (r_i(t) - r_i(0))^2 = 6Dt \quad \text{eq.2}$$

where D is the diffusion coefficient in three-dimension.

Equilibrated doping structures from MC simulation at 300 K are used and further equilibrated at diffusion temperatures (1273 K, 1473 K, 1673 K, 1873 K and 2073 K) under NVT condition for 1 ns. The MSD data are collected in another 1 ns production stage. The obtained MSD are averaged over three independent configurations with different initial velocities. 1273 K is the lowest temperature in our case to observe significant O^{2-} ion diffusion, therefore no lower temperature was sampled here.

A nudged elastic band (NEB) calculation implemented in LAMMPS is used to obtain the O^{2-} diffusion energy barrier. The time step for the damped dynamics minimization used in NEB calculation is set to be 0.5 fs, which is half of the 1 fs used in normal MD simulation due to the irregular potential energy surface at the GB. The spring constant for the parallel nudging force has been varied to ensure the convergence of the calculated energy barrier.

3. Results and discussions

3.1. La^{3+} segregation

In order to study the most stable sites for the dopants, La^{3+} and Y^{3+}, in YSZ, a Σ13(510)/[001] GB structure was constructed and the dopant distribution compared for, both, 10YSZ alone and 8.5Y1.5LaSZ. Figures 1a and 1b show the equilibrated GB configuration of 10YSZ and 8.5Y1.5La, respectively. Anions are perturbed more from their lattice positions at the GB region than cations. Y^{3+} appears uniformly distributed in both structures, while La^{3+} shows a significant preference for the GB. To quantify this, a density profile is determined to show the numbers of ions of each element in planes at different distances to GB (Figure 1c and 1d). The density is an averaged number of ions on one $lx \times lz$ plane with a bin size of 3 Å along the y axis. To ensure statistical significance, the profile is averaged over 3 independent configurations, for each configuration we generated 40 equilibrated structure snapshots uniformly sampled within 2×10^7 MC steps.

As seen from Figure 1c, both O^{2-} and Zr^{4+} density profiles show a minimum at the GB. This is similar to what occurs for a non-doped ZrO_2 GB structure (Supporting Figure S1), which is attributed to an inherent nature of GB regions. Y^{3+} however, has a constant density over the whole structure, which results in a higher Y^{3+}/Zr^{4+} ratio at the GB itself, with 0.33 averaged over the two GB regions at Zr^{4+} valleys as compared to 0.225 in the bulk phase (a segregation factor of 1.47). This is consistent with previous simulations [20], in which Lee et al. obtained a segregation factor of 1.2 in a Σ5(310)/[001] structure with the same doping concentration, and an experimental value of 1.5 as an average value over different GBs [25].

In the presence of La^{3+}, a significant peak of La^{3+}occurs at the GB, while O^{2-} and Zr^{4+} density profiles remain the same. Interestingly, Y^{3+} density decreases at the GB. This indicates the segregation energy of La^{3+} is higher than Y^{3+} so that it replaces Y^{3+} in the GB region. This is

confirmed by our calculation of segregation energies from their lattice positions at GB of various dopants (Supporting Information Figure S2) as well as previous studies [9]. The averaged (Y^{3+} + La^{3+})/Zr^{4+} ratio at GB is 0.304 and 0.223 in bulk, leading to a total segregation factor of 1.38. The substitution of Y^{3+} by La^{3+} at the GB thus decreases the total segregation factor, what can be understood by the fact that La^{3+} has a larger ionic radius as compared to Y^{3+}, thus occupying a larger volume.

3.2. GB energies

Several GB structures either in [001] tilt or [110] tilt directions have been constructed to calculate the effect of La^{3+} segregation on the respective GB energies. For comparison, both 10YSZ and 8.5Y1.5La were studied using similar GB misorientations. La^{3+} segregation is observed in all constructed GB structures (Supporting Figure S3). The grain boundary energy of each GB structure was calculated from the potential energy difference between the GB structure and the corresponding bulk structure, which is obtained under NVT condition (the volume is fixed after relaxing the ZrO_2 GB structure at zero pressure). The calculated GB energy is an average of 3 independent configurations (Figure 2a). The first two tilt angles (22.69^0 and 36.9^0) are in the [001] tilt direction, and others are based on the [110] tilt axis. First of all, the obtained GB energy of 10YSZ is reasonably close to previous experimental results for 8YSZ (Table 2) [26]. The most stable obtained GB configuration is Σ11(113), consistent with experimental results [26]. The configuration with the highest GB energy in our simulation is Σ3(112), instead of Σ11(332) in experiments. It is worth mentioning that in experiments, the GB energy is the Gibbs free energy that also considers volume expansion and entropy. We examined the contribution of volume expansion by further

relaxing the equilibrated Σ13(510) doped structure at constant ambient pressure, and found it only contributes 0.2% of internal energy. Neglecting entropy could lead to the difference.

Table 2 GB energy comparison between simulation value and literature experimental value of several [110] tilted structures

GB structure ([110] tilt)	Simulation 10YSZ (J/m^2)	Experiments 8YSZ (J/m^2)[26]
Σ11(332)	1.16 ± 0.05	0.95 ± 0.25
Σ3(111)	0.54 ± 0.12	0.48 ± 0.25
Σ3(112)	1.64 ± 0.10	0.59 ± 0.15
Σ11(113)	0.18 ± 0.19	0.32 ± 0.08
Σ9(114)	1.3 ± 0.14	0.8 ± 0.1

For all sampled GB structures, La^{3+} doping decreases the GB energy. The average decrease is 0.25 J/m^2, which is reasonable comparing to the experimental measurements GB energy decrease value ~0.5 J/m^2 (from 12YSZ to 10Y2La doped case) [6]. In order to understand this energy decrease, the GB energy is decomposed into the elements, as shown in Figure 2b, using Σ13(510)/[001] as an example. For both, the 10YSZ and the La-doped case, Zr^{4+} and Y^{3+} show a positive value, which means they have a higher energy in the GB structure than in bulk. On the other hand, O^{2-} and La^{3+} contribute negatively, which means the species energies are lower in a GB configuration. Comparing the difference between 10YSZ and the La-doped case, we find for all species the GB energy is decreased with La^{3+} doping, and thus the whole structure shows a lower GB energy and is more stable. In order to extend the analysis to different structures, we separate cations and anions, and show their contribution to GB energy change with La^{3+} doping (Figure 2c). The GB energy difference is defined as the GB energy of 10YSZ minus the GB energy of 8.5Y1.5La, which is represented by the delta column in Figure 1a Thus, the positive GB energy difference means 10YSZ has higher GB energy than 8.5Y1.5La, which is the case for cations in all the structures. On the other hand, the anion GB energy is dependent on the GB configuration. The two [001] tilt cases show anion GB energy is higher in 10YSZ, while the [110] tilt structures

lead to the opposite conclusion. However, since the stabilization effect of cations dominates over anions, the total GB energy is decreased in all cases.

Apart from the grain boundary energy, the energetic homogeneity of nanocrystalline YSZ could also be important to determine materials properties. To visualize the energy distribution with different dopants, 2-dimensional energy fluctuation maps are plotted in Figure 3. The fluctuation value at each lattice point is its potential energy difference to the averaged value over the same element in the whole structure. The energy grain size and shape is determined by Voronoi tessellation, i.e., any point in an atom's Voronoi cell is closer to that atom than any other. 20 snapshots uniformly sampled within the 10^7 MC steps of analysis were used to make one map for each configuration and results of the most representative configurations are presented here. Maps of other configurations are included in Supporting Information (Figure S4 and S5).

Figures 3a and 3b show the energy fluctuation map for 10YSZ bulk. As expected, the energy maps reflect a homogeneous structure with relative low fluctuations caused by thermal energy. With GBs, a heterogeneous energy region is evident which marks the GB area (Figure 3c-f). High energy spots are centered along the GB plane, which implies the unstable nature of GB compared to bulk. However, with La^{3+} doping, some high energy spots have been smoothed out, and the GB morphology becomes less distinct to its bulk phase. This conclusion is verified by choosing different snapshots during the equilibration stage (Fig. S4a and S4b), where the fluctuation map shows the same distribution with slightly different fluctuation values. Results between different configurations were also compared (Fig. S4c and Fig. S5). Although different high fluctuation regions could be observed at GB for the same doping condition, La^{3+} doping shows in general fewer high energy regions. Such dampening of the concentrated excess energies at the grain

boundary regions is expected to be responsible for lowering the driving force for coarsening of YSZ, as observed experimentally [4].

3.3. Oxygen ion diffusion coefficient

In order to evaluate the role of the observed La^{3+} segregation on the ionic conductivity of YSZ, the Σ13(510)/[001] GB structure was selected due to its abundance in polycrystalline materials [27] for the subsequent diffusion study involving MSD of O^{2-} at different temperatures in both 10YSZ and 8.5Y1.5La. Cations were found to not diffuse within this temperature range and only vibrate around lattice positions, as no cation vacancies exist in addition to the high activation energy [28]. Good linearity of the MSD with time was observed (Supporting Figure S6) for the 1273 K to 2073 K temperature range and fitted diffusion coefficients are shown in Figure 4a. Lower temperatures were not sampled here due to lack of significant diffusion.

The GB region was defined as the area occupied by La^{3+} segregation, as marked in yellow in Figures 1c and 1d (± 6 Å from GB center along y axis). Conversely, the bulk region is the rest of the structure. From Figures 4a and Figure S6a, one observes faster diffusion of O^{2-} in 10YSZ as compared to 8.5Y1.5La for both, bulk or GB regions. The diffusion coefficient is higher in the bulk region as compared to the GB region, and anisotropic diffusion occurs in the GB region, where in the y direction (perpendicular to GB plane) a lower MSD rate is observed in contrast to both x and z directions (Figure S6b and S6c).

As seen in Figure 4a, good linearity in an Arrhenius plot for the bulk data for both 10YSZ and 8.5Y1.5La is observed and represents a single activation energy E for diffusion, which is fitted to be 0.85 eV for 10YSZ and 0.8 eV for 8.5Y1.5La, with pre-exponential factors D_0=7x10^{-9} m^2/s and 4.5x10^{-9} m^2/s, respectively. The results are for pure Y doping close to E ~1.0 eV for 10YSZ from

experiments [29], and previous simulations for D_0 and in E in crystal 8YSZ ~5.8 x10^{-9} m^2/s and 0.6 eV [17, 30]. 10YSZ and 8.5Y1.5La show very close activation energies for bulk diffusion. This is reasonable as La^{3+} only segregates in the GB region and does not significantly affect the cation distribution in the bulk.

In the GB region, the linear correlation is not well defined, which is possibly due to the existence of multiple activation energies. Considering the inhomogeneous potential energy distribution in the GB area (Figure 3), it is likely that different lattice sites can lead to different diffusion barriers and will be discussed further in the following discussions.

La^{3+} doping concentrations were then varied to better understand the influence of the dopant on the grain boundary oxygen transport. Apart from 10YSZ and 8.5Y1.5La, 9.5Y0.5La, 9Y1La, 8Y2La, 7Y3La, 6Y4La and 5Y5La structures were generated and the results are shown in Figure 4b. La^{3+} segregation occurs in all cases, and the dopant density distribution of the highest La^{3+} doping (5% molar fraction) is shown in Supporting Figure S7. From Figure 4b, unlike Y^{3+} doping where an optimal doping concentration exists for fastest diffusion, the diffusion coefficient monotonically decreases with the increasing La^{3+} concentration, and the decrease becomes more important with increasing temperature.

3.4. Van Hove correlation analysis

In order to understand the observed diffusion behavior, the van Hove correlation function G(r,t) [31, 32] was first analyzed for O^{2-}. It is represented by a self $G_s(r,t) = \frac{\sum_j \delta(r+r_j(0)-r_j(t))}{N_j}$, and a distinct $G_d(r,t) = \frac{\sum_{i\neq j} \delta(r+r_i(0)-r_j(t))}{N_i}$ part. The self-correlation part compares the original position of an ion to its position at a different time, which reflects the motion pattern of the ion

relative to itself. The distinct part compares the position of an ion to the position of other ions at a different time, and thus reveals information of correlated motions. The calculated G_s and G_d for O^{2-} at 2073 K are presented in Figures 5 and 6 to highlight the most significant changes.

In a liquid, G_s has the form of a Gaussian distribution and its peak moves towards longer distance and approaches zero with time [30]. This behavior is not observed in our case. Instead, distinct peaks keep emerging at longer distance, accompanied by the decrease of former peaks (Figure 5). The first peak represents the original positions, the second peak corresponds to the nearest neighbor distance of O^{2-} in fluorite structure, and third peak is at O^{2-} second nearest neighbor position and so on. Therefore, the diffusion is essentially a hopping process of O^{2-} among its lattice positions. Comparing the pattern in the bulk and the GB region (Figs. 5a-d), the decrease rate of former peaks is higher in the bulk than in the GB, which means O^{2-} has a higher hopping rate in the bulk region. This is consistent with our previous conclusion that the diffusion coefficient is higher in the bulk region. If comparing 10YSZ and 8.5Y1.5La, first the peak decrease rate is similar in the bulk (Fig. 5a and 5c), but much lower in the GB area with La^{3+} doping, which also confirms previous conclusions regarding diffusion rates. Second, the peak becomes less distinguishable in the 8.5Y1.5La GB area (Fig. 5bd), which indicates a more perturbed crystal structure. As La-O has a longer bond length (2.35 Å) as compared to Y-O (2.25 Å) and Zr-O (2.05 Å) at the GB region (Supporting Figure S8), it is reasonable to assume the anions will make more position adjustments to accommodate La^{3+}.

At t=0, G_d is essentially the same as the radial distribution function of the oxygen-oxygen pair. With increasing time, oxygen ions begin to migrate into other oxygen ion's initial spots, which leads to the initial increase of the first peak in Figure 6. Unlike G_s, the peak will eventually

maintain the same magnitude when O^{2-} ions are uniformly distributed in the structure. Thus, the change rate of peak magnitude on one hand reflects the hopping rate, and on the other hand also indicates the oxygen vacancy distribution. Comparing the bulk and GB region (Figs. 6ab vs Figs. 6cd), one reason for faster increasing rate in the bulk region is due to higher hopping rate, as revealed from G_s. An alternative explanation could be related to inhomogeneous distribution of oxygen vacancies at the GB. When comparing 10YSZ and 8.5Y1.5La in the bulk region (Figs. 6a and 6c), as their hopping rate should be similar from the study of G_s, the lower peak change rate in La^{3+} doped case should indicate a less homogeneous distribution of oxygen vacancies. Similarly, in the GB region (Fig. 6b and 6d), the increase rate of the first peak is much lower with La^{3+} doping than in 10YSZ, which can be both due to low hopping rate and inhomogeneity.

3.5. Dopant-vacancy binding energy and hopping energy barriers

As seen from the van Hove analysis, the O^{2-} diffusion is dominated by hopping energy barriers and oxygen vacancy distribution. The diffusion energy barrier could come from both the energy of moving oxygen vacancies from the dopant, as defined by dopant-vacancy binding energy, and the activation energy along the migration path itself. Therefore, both energies are calculated in Figure 7 to quantify the energetic difference in 10YSZ and 8.5Y1.5La.

The dopant-vacancy binding energy is first calculated in a pure ZrO_2 bulk structure, where two dopants and one oxygen vacancy is created. The two dopants position are fixed (one dopant is kept 2.5 nm away from the oxygen vacancy). By plotting the potential energy change of the whole structure with moving the oxygen vacancy away from one dopant position (Figure 7a), it shows a higher binding energy with La^{3+} (-0.60 eV) comparing to Y^{3+} (-0.55 eV), which occurs both at the second nearest neighbor positions.

As most La^{3+} ions are at the GB, the binding energy at the GB region is also considered. The difference in the binding energy at the GB may come from the structural discontinuity along the y direction. The lattice positions in the xz plane are similar to bulk phase, only being more perturbed. Therefore, we selected one dopant near the center of the GB (shown in the inset of Figure 7b) and moved oxygen vacancies away from it in the y direction. The GB structure shown in the figure is before minimization for a clearer view. The structure used for calculation is the one after minimization and relaxation. All possible O^{2-} sites along the path in y axis are considered and each energy point is the average over the trial results at the same dopant-vacancy distance range. The grain size is around 5.2 nm, and to avoid another GB's influence, the longest sampled distance was 3 nm. From Figure 7b, one observes the potential energy well is much deeper than in the bulk, as the movement of the oxygen vacancy away from the grain boundary already leads to an energy increase. The energy change measured here is not the pure binding energy, however this quantity is directly related to the diffusion energy barrier and thus we just consider it as a whole. Apparently, oxygen vacancies are much harder to diffuse across GB than in bulk. Moreover, La^{3+} doping decreases the depth of the potential well as compared to Y^{3+}, indicating a smaller dopant-vacancy binding energy. This effect is attributed to the free space at the GB which makes La^{3+} less prone to energetically require a vacancy nearby to accommodate itself as in the bulk structure.

The above discussed binding energies are essentially the energy barriers for diffusion in an inhomogeneous structure, i.e., the defects in the structure such as the GB or the dopants and vacancies are not uniformly distributed and the redistribution of anions will lead to an energy change. Nevertheless, the hopping of anions between lattice points itself has an energy barrier

and requires further characterization. Migration energy is then calculated for both bulk and GB case using the NEB method [33, 34] (Figs 7cd, the insets indicate the hopping sites). Figure 7c shows the O^{2-} migration energy around Y^{3+} to be 0.8 eV in a perfect ZrO_2 bulk phase, which is consistent with our previous fitted diffusion energy barrier (Figure 4a). La^{3+} leads to a higher migration energy of 1.2 eV. The hopping energy at the GB is complicated, as many different sites can lead to different migration energies. As the average property of different spots can be reflected in the diffusion study (section 3.3), here two spots were chosen for hopping across GB to illustrate the difference (Figure 7d and Supporting Figure S9). In both cases, the migration energy at the GB is higher than in bulk, and this explains the lower diffusion coefficient at the GB in section 3.3. Besides, La^{3+} leads to a higher migration energy, as in Figure 8d the barrier is 2.1 eV comparing to 1.8 eV for Y^{3+}, and 1.6 eV in Figure S9 comparing to 1.4 eV for Y^{3+}. Combined with results from section 3.3, La^{3+} hinders O^{2-} hopping process, and multiple energy barriers exist due to structure inhomogeneity.

3.6. Discussion of the results and model accuracy

Dynamic studies of O^{2-} diffusion in section 3.3 reveal the lower diffusion coefficient at the GB area comparing to the bulk, and this has been explained by both the higher binding energy and migration energy barrier at GB in section 3.5. Multiple activation energies depending on the lattice sites at the GB were found which lead to the non-linear behavior in the Arrhenius plot for the GB case. With La^{3+} segregation, it disfavors the diffusion process as the migration energy barrier is higher, although it seems to decrease the binding energy with oxygen vacancy at the GB.

The simulation model captures the essential structure and energy change with La^{3+} doping. One must note that there are several factors not being considered in this model when using this data to interpret experimental tests on ionic conductivity. First of all, the diffusion of O^{2-} at low temperature (below 973 K) is very hard to observe in the simulation, especially at the GB region, and cations are not able to diffuse even at 2073 K due to short simulation timescale and very high energy barrier. Noteworthy, in real systems, the dopant distribution at the GB and even the GB morphology is expected to change at the temperature we set for diffusion, since grain growth already takes place at temperatures as low as 900 ^{0}C [6]. Secondly, the energy barrier calculations are all done in the extreme dilute doping concentration (only two dopants and one oxygen vacancy). For the bulk area, the result may not differ too much since the studied concentration ensures a dispersed distribution of dopants and vacancies. The GB region, however, could be different due to the segregation of dopants in the relative small area. The presence of other dopants and vacancies may affect the migration barrier.

4. Conclusions

In summary, this study characterized the La^{3+} segregation phenomena at GB in YSZ, and revealed the GB energy can be reduced by 0.25 J/m^2 as an average over eight GB structures with different tilt direction and tilt angles. The energy decrease of cations by La^{3+} segregation in the structure was found to be the main reason for the GB stabilization, while anions energy could either increase or decrease depending on the GB misorientation. It was also found that high energy fluctuation spots are observed around the GB, which could be smoothed out with La^{3+} doping, and makes GB less energetically distinguishable from the bulk. The O^{2-} diffusion study on Σ13(510)/[001] structure reveals La^{3+} mainly decreases diffusion coefficient at the GB region

(± 6 Å from GB center), while it has little impact on the bulk area. The diffusion coefficient decreases with increasing La^{3+} concentration, and this effect becomes more dominant at higher temperature. van Hove correlation function shows the O^{2-}diffusion process is mainly by hopping from lattice sites, and La^{3+} doping potentially leads to a less homogenous distribution of oxygen vacancies. The diffusion activation energy come from both the dopant-vacancy binding energy and hopping energy barrier, and energetic study under dilute doping condition in ZrO_2 further revealed La^{3+} has higher binding energy with oxygen vacancy in the bulk comparing to Y^{3+}, but lower binding energy at GB. Meanwhile, it also leads to higher hopping energy both in bulk and GB area than Y^{3+}, and the hopping energy barrier depends on the exact lattice position selected. Therefore, the diffusion of O^{2-} in the GB structure has multiple activation energies and La^{3+} generally hinders its diffusion.

5. Acknowledgements

This research was supported by the U.S. Department of Energy, Office of Nuclear Energy, Nuclear Energy University Program under Grant No. DE-NE0000704. RC also thanks Army Research Office, W911NF-17-1-0026.

References

1. H. L. Tuller, *Solid State Ionics*, 2000, 131, 143-157.
2. H. Huang, M. Nakamura, P. Su, R. Fasching, Y. Saito and F. B. Prinz, *J. Electrochem. Soc.*, 2007, 154, B20-B24.
3. P. C. Millett, R. P. Selvam and A. Saxena, *Acta Mater.*, 2007, 55, 2329-2336.
4. J. Weissmüller, *Nanostruct. Mater.*, 1993, 3, 261-272.
5. J. Weissmüller, *J. Mater. Res.*, 1994, 9, 4-7.
6. S. Dey, C.-H. Chang, M. Gong, F. Liu and R. H. R. Castro, *J. Mater. Res.*, 2015, 30, 2991-3002.
7. N. Nafsin and R. H. R. Castro, *J. Mater. Res.*, 2017, 32, 166-173.
8. T. Oyama, M. Yoshiya, H. Matsubara and K. Matsunaga, *Phys. Rev. B: Condens. Matter*, 2005, 71, 224105.
9. T. Yokoi, M. Yoshiya and H. Yasuda, *Langmuir*, 2014, 30, 14179-14188.
10. H. B. Lee, F. B. Prinz and W. Cai, *Acta Mater.*, 2010, 58, 2197-2206.
11. C. A. J. Fisher and H. Matsubara, *Solid State Ionics*, 1998, 113-115, 311-318.
12. R. L. González-Romero, J. J. Meléndez, D. Gómez-García, F. L. Cumbrera and A. Domínguez-Rodríguez, *Solid State Ionics*, 2013, 237, 8-15.
13. R. L. González-Romero and J. J. Meléndez, *J. Alloys Compd.*, 2015, 622, 708-713.
14. R. Krishnamurthy, Y. G. Yoon, D. J. Srolovitz and R. Car, *J. Am. Ceram. Soc.*, 2004, 87, 1821-1830.
15. D. S. Aidhy, Y. Zhang and W. J. Weber, *The Journal of Physical Chemistry C*, 2014, 118, 4207-4212.
16. C. A. J. Fisher and H. Matsubara, *J. Eur. Ceram. Soc.*, 1999, 19, 703-707.
17. R. Devanathan, W. J. Weber, S. C. Singhal and J. D. Gale, *Solid State Ionics*, 2006, 177, 1251-1258.
18. X. Xie, R. V. Kumar, J. Sun and L. J. Henson, *J. Power Sources*, 2010, 195, 5660-5665.
19. M. O. Zacate, L. Minervini, D. J. Bradfield, R. W. Grimes and K. E. Sickafus, *Solid State Ionics*, 2000, 128, 243-254.
20. H. B. Lee, F. B. Prinz and W. Cai, *Acta Mater.*, 2013, 61, 3872-3887.
21. J. A. Dawson and I. Tanaka, *Langmuir*, 2014, 30, 10456-10464.
22. J. A. Dawson and I. Tanaka, *Journal of Materials Chemistry A*, 2014, 2, 1400-1408.
23. S. Plimpton, *J. Comput. Phys.*, 1995, 117, 1-19.
24. M. G. Martin, *Molecular Simulation*, 2013, 39, 1212-1222.
25. A. J. A. Winnubst and A. J. Burggraaf, *Mater. Res. Bull.*, 1984, 19, 613-619.
26. N. Shibata, F. Oba, T. Yamamoto and Y. Ikuhara §, *Philosophical Magazine*, 2004, 84, 2381-2415.
27. G. S. Rohrer, *Journal of Materials Science*, 2011, 46, 5881.
28. R. L. González-Romero, J. J. Meléndez, D. Gómez-García, F. L. Cumbrera, A. Domínguez-Rodríguez and F. Wakai, *Solid State Ionics*, 2011, 204-205, 1-6.
29. M. Kilo, C. Argirusis, G. Borchardt and R. A. Jackson, *PCCP*, 2003, 5, 2219-2224.
30. L. Kah Chun and I. D. Brett, *J. Phys.: Condens. Matter*, 2011, 23, 035401.
31. B. Smit, *Understanding molecular simulation: from algorithms to applications*, Academic Press, 1996.

32. D. C. Rapaport, *The art of molecular dynamics simulation*, Cambridge university press, 2004.
33. G. Henkelman, B. P. Uberuaga and H. Jónsson, *J. Chem. Phys.*, 2000, 113, 9901-9904.
34. G. Henkelman and H. Jónsson, *J. Chem. Phys.*, 2000, 113, 9978-9985.

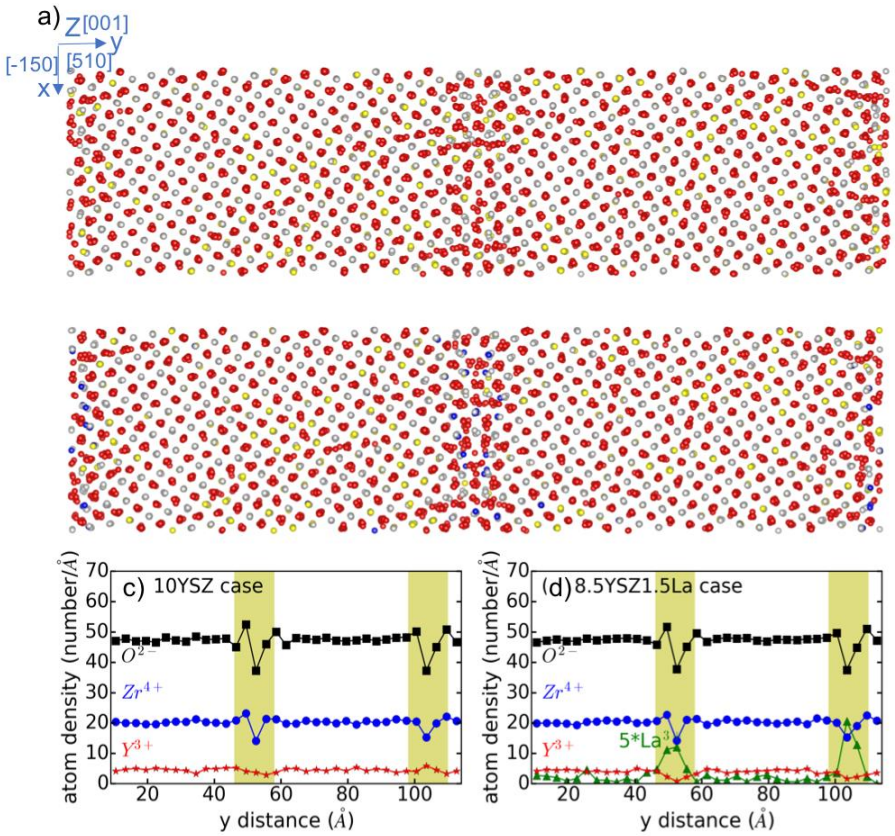

Figure 1 Equilibrated Σ13 (510)/[001] configuration of a) 10YSZ and b) 8.5Y1.5La at 300 K, with one GB at the center (y=52 Å) and the other GB at the border of simulation box (y=0 and y=104 Å; Corresponding element density distribution where GB regions are marked yellow (± 6 Å); c) 10YSZ d) 8.5Y1.5La. La^{3+} density has been magnified 5 times for easier comparison.

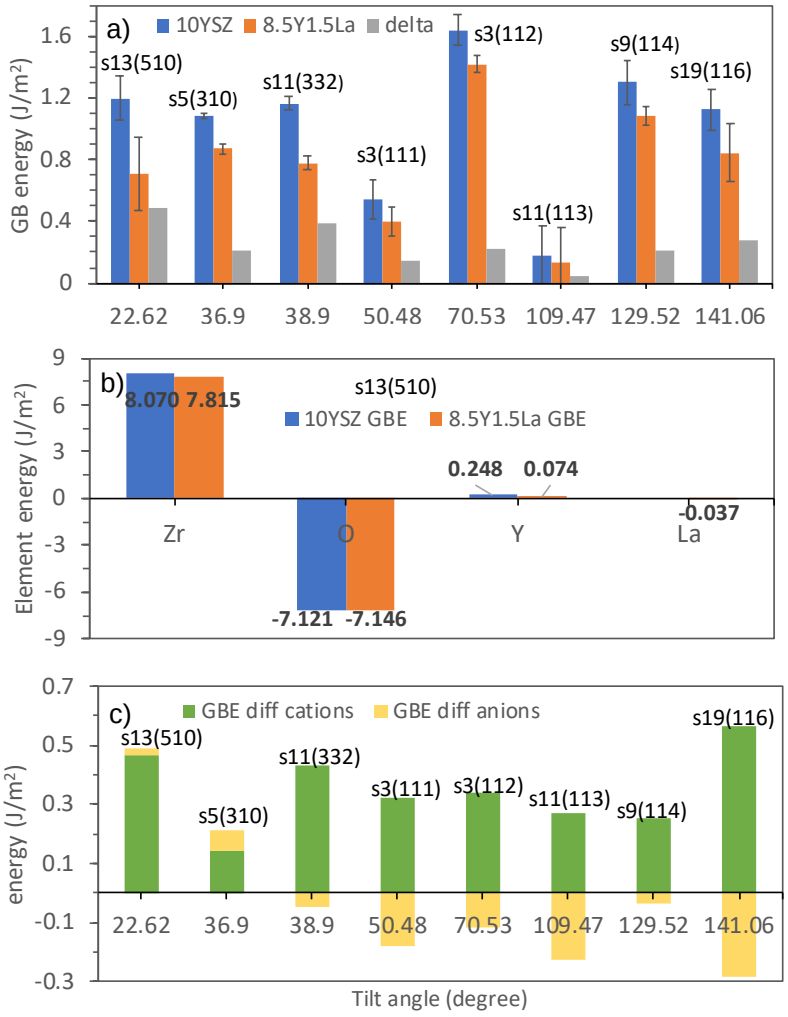

Figure 2 a) GB energy for different tilt angles, delta is the GB energy difference between 10YSZ and 8.5Y1.5La. Error bars are obtained from three independent samples. b) GB energy decomposed to different elements in Σ13 (510)/[001] c) GB energy difference decomposed to cations and anions, the GB energy difference is the delta value in a).

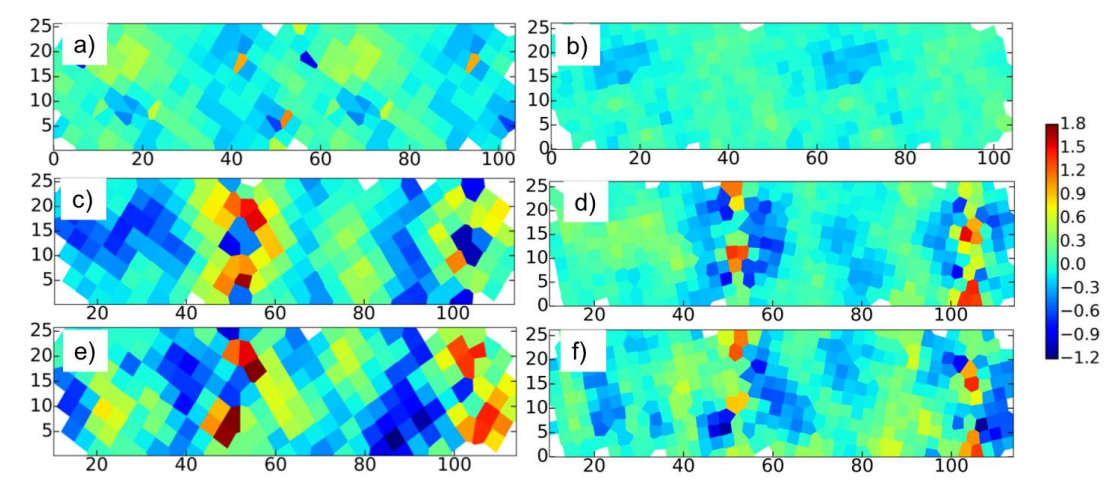

Figure 3 Two-dimensional potential energy fluctuation map (eV/atom) with Voronoi tessellation, representing the deviation of the potential energy inside the crystallite lattice from the average energy in each system for cations (Zr^{4+}, Y^{3+}, La^{3+} if any) and anions (O^{2-}). The average potential energies for all types of ions in each structure are reported in ***Table S2****. a) Cations and b) Anions energy fluctuation in 10YSZ bulk structure. c) Cations and d) Anions energy fluctuation in 10YSZ GB structure. e) Cations and f) Anions energy fluctuation in 8.5Y1.5La GB structure.*

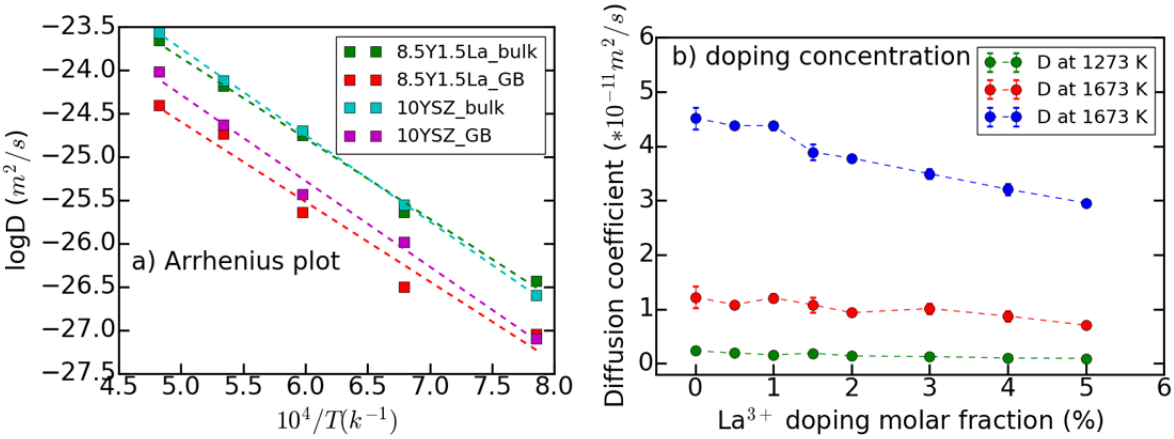

Figure 4 a) Arrhenius plot for GB and bulk region diffusion coefficient in 10YSZ and 8.5Y1.5La configuration. b) Diffusion coefficient change with different La_2O_3 doping molar fraction, and the data is averaged from 3 independent configurations with different initial velocities. Some error bars are smaller than the marker.

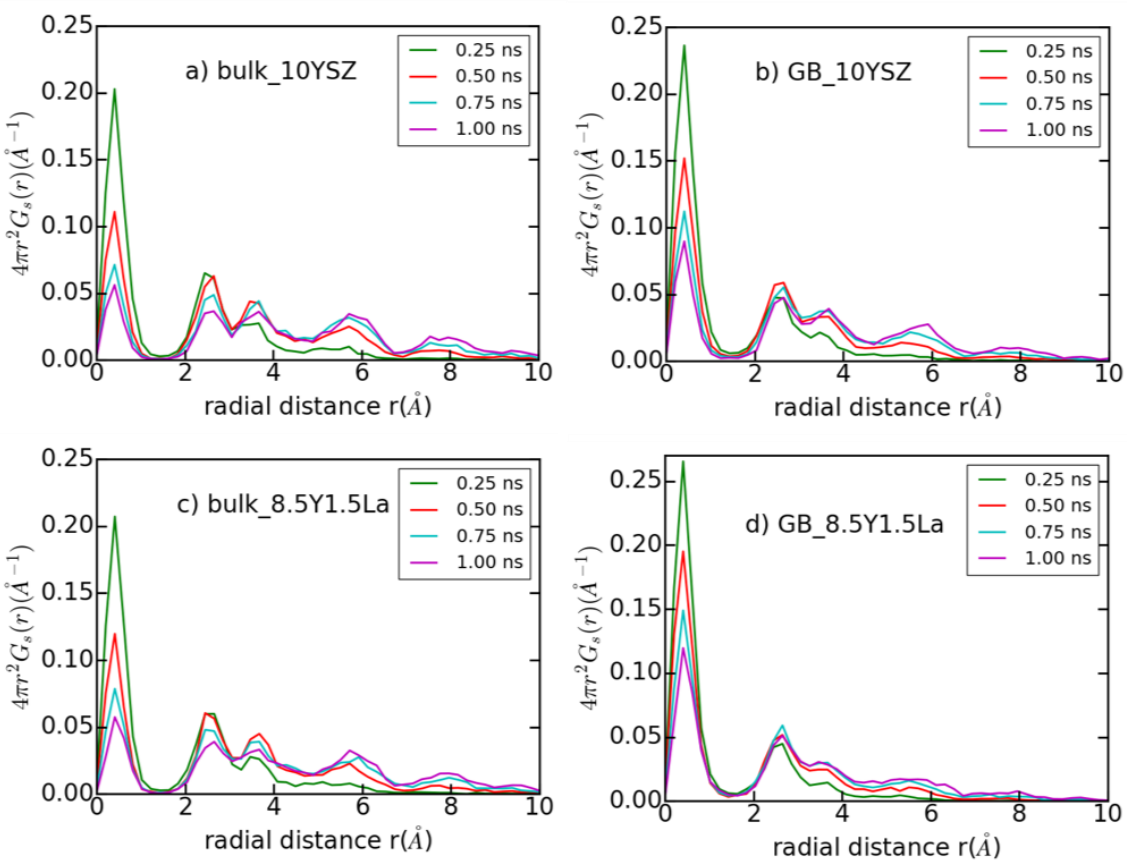

Figure 5 Self correlation part in van Hove function for oxygen ions at 2073 K in a) bulk 10YSZ; b) GB 10YSZ; c) bulk 8.5Y1.5La; d) GB 8.5Y1.5La. The bulk and GB regions are the same as in Figure 4. Each curve is time averaged within 0.25 ns period.

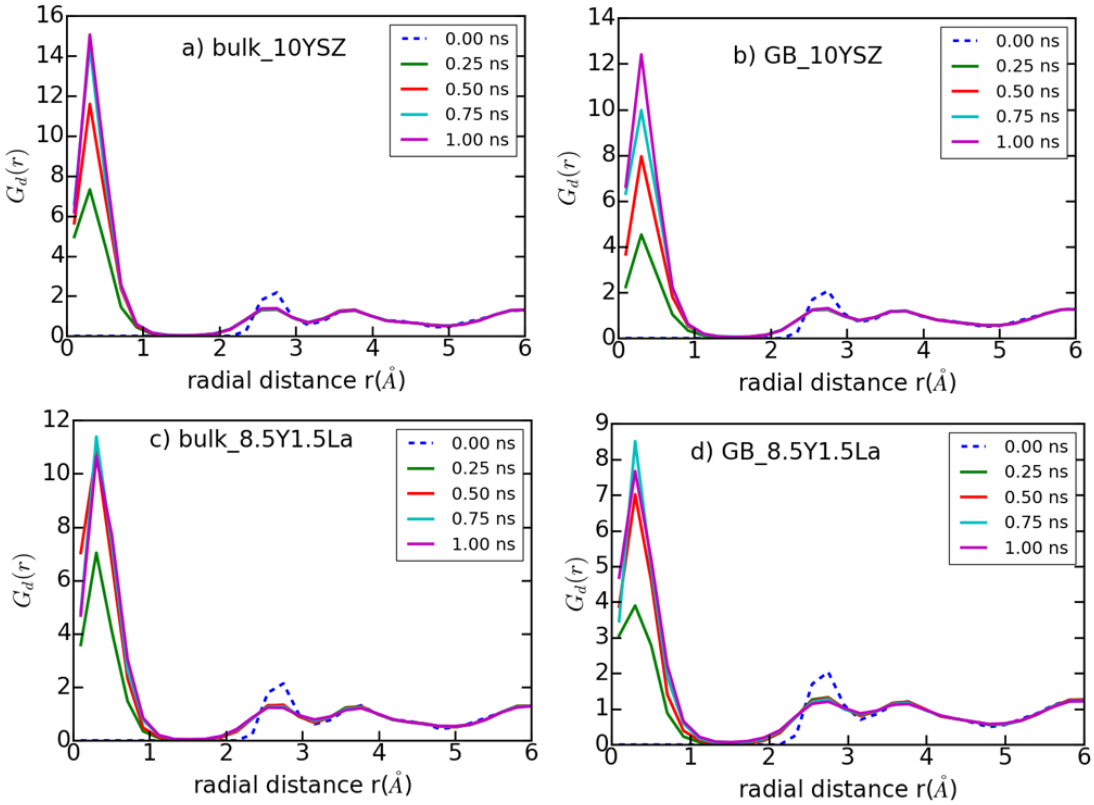

Figure 6 Distinct correlation part in van Hove function for oxygen ions at 2073 K in a) bulk 10YSZ b) GB 10YSZ c) bulk 8.5Y1.5La d) GB 8.5Y1.5La. The bulk and GB regions are the same as in Figure 4. Each curve is time averaged within 0.25 ns period, except for t=0.

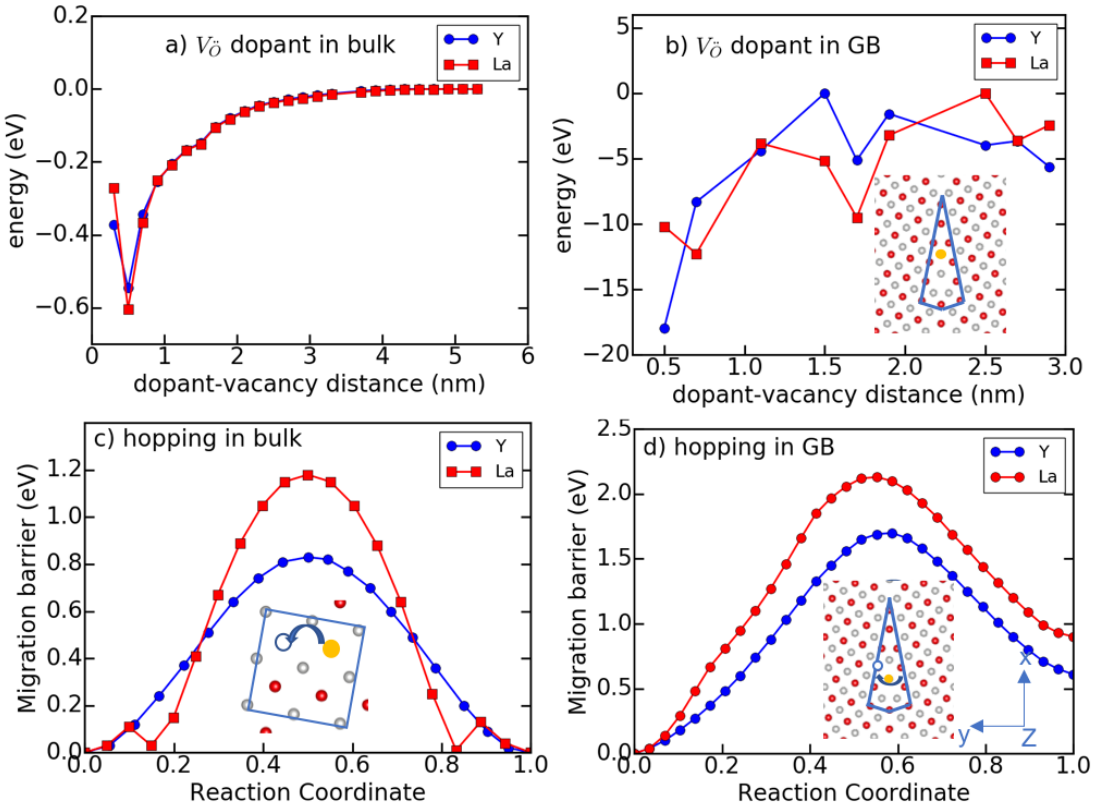

Figure 7 vacancy-dopant binding energy in a) bulk; b) Σ13(510)/[001] ZrO_2 GB region. Energy is shifted to zero with respect to the highest energy value. NEB calculation for hopping energy barrier in c) bulk; d) GB region along y axis. The insets show the oxygen vacancy or dopant positions, where blue lines mark the GB unit cell in b) and d), and the fluorite unit cell in c). Color representation in the insets: void blue circle: oxygen vacancy; yellow: trivalent dopant; red: O^{2-}; grey: Zr^{4+}.